Treelike Interactions and Fast Scrambling with Cold Atoms: Supplemental Material

(Dated: August 11, 2019)

In this supplement, we elaborate on the proposed experimental implementation and on numerical and analytical techniques used to obtain the results in the main text. In Section I we discuss details of the experimental implementation including the effects of dissipation. In Section II we explain the methods used to find upper and lower bounds on magnon occupation growth times t_ϵ, present evidence for chaotic level statistics, discuss the short-time expansion of OTOCs, and elaborate on the semiclassical and Matrix-Product State numerical methods used in the main text.

I. EXPERIMENTAL IMPLEMENTATION

A. Engineering the Couplings

We propose an experimental implementation in a one-dimensional array of atoms uniformly coupled to the mode of an optical cavity, with vacuum Rabi frequency $2g$. At each of N sites are n atoms that encode a spin of length $S = nF$, either in the Zeeman states of an individual spin-F atom ($n = 1$) or in the collective magnetization of a localized ensemble. A magnetic field gradient produces a Zeeman splitting $\omega_Z + j\omega$ that depends linearly on the site number $j \in \{1, \ldots, N\}$. Spin-exchange interactions are introduced by an optical control field at large detuning Δ from atomic excited states, as in Ref. [1]. This control field, with center frequency ω_0, drives virtual Raman processes wherein an atom absorbs a photon and emits it into the cavity mode at frequency ω_c, whence it is rescattered by another atom.

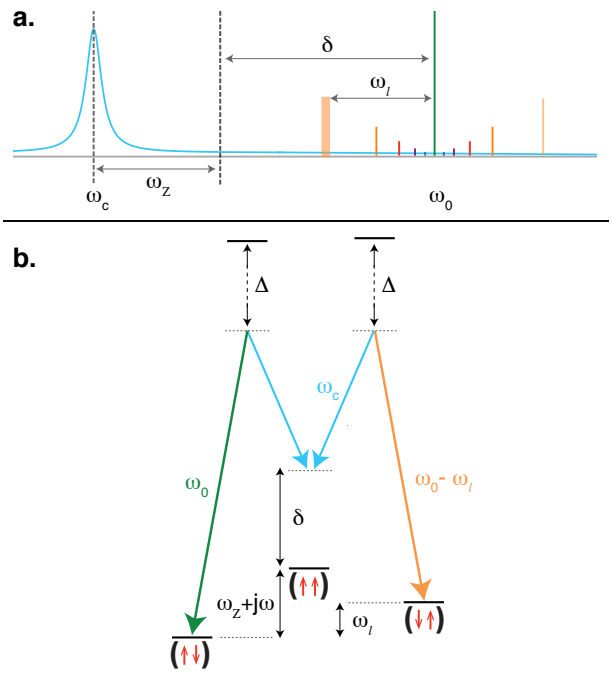

FIG. S1: **Experimental implementation.** (a) Spectrum of frequencies: cavity resonance, Raman resonance, and a set of drive fields for $s > 0$ are sketched. The drive field corresponding to the particular four-photon process depicted in (b) is shown in bold. (b) Photon-mediated spin-exchange in a magnetic field gradient. A photon is absorbed from the carrier at ω_0 and exchanged with another atom via the cavity mode at frequency ω_c, followed by emission into a sideband at $\omega_0 - \omega_\ell$.

To turn on interactions at each distance $d = 2^\ell$, the control field is amplitude-modulated at frequency ω_ℓ and modulation index $\beta_\ell \ll 1$ to generate sidebands of Rabi frequencies $\Omega_\ell = \beta_\ell \Omega_0$, where Ω_0 is the Rabi frequency of the carrier. We assume that the detuning $\delta = \omega_0 - \omega_c - \omega_Z$ of the carrier from Raman resonance is large compared to all modulation frequencies and to the cavity linewidth κ, i.e., we assume $\delta > (\log_2 N)\omega$ and $\delta > \kappa$. The spin-exchange

couplings are then given by

$$J(d=2^\ell) \propto \frac{n\Omega_\ell\Omega_0 g^2}{\Delta^2\delta}, \tag{S1}$$

where n is the number of atoms per site.

B. Effects of Dissipation

To calculate how coherent the interactions can be, we would like to compare the couplings J with the rates of two decay processes: collective decay via photon loss from the cavity mode and single-atom decay due to spontaneous emission. To this end, we start by re-expressing the interaction strengths in terms of the free-space scattering rate due to the control field carrier,

$$\Gamma_{\mathrm{sc},0} = \frac{\Omega_0^2}{4\Delta^2}\Gamma, \tag{S2}$$

where Γ is the atomic excited-state linewidth. In terms of $\Gamma_{\mathrm{sc},0}$ and the single-atom cooperativity $\eta = 4g^2/(\kappa\Gamma)$, we have

$$J(d=2^\ell) \sim \beta_\ell n\eta\frac{\Gamma_{\mathrm{sc},0}\kappa}{\delta}, \tag{S3}$$

which shows that interactions can dominate over spontaneous emission for sufficiently large cooperativity $n\eta$. Below, in identifying requirements on the cooperativity, we will keep in mind that the total spontaneous emission rate is augmented by the power in the sidebands: $\Gamma_{\mathrm{sc}} = B\Gamma_{\mathrm{sc},0}$, where $B = 1 + 2\sum_\ell |\beta_\ell|^2$.

A second dissipation mechanism is photon loss from the cavity. Cavity decay leads to collective dissipation described by a set of Lindblad operators

$$L_{k,\pm} = \sqrt{\gamma_{k,\pm}}S_k^\pm, \tag{S4}$$

where we have defined the spin-wave operators

$$\mathbf{S}_k = \frac{1}{\sqrt{N}}\sum_{j=1}^{N} e^{ikx_j}\mathbf{S}_j. \tag{S5}$$

The decay rates $\gamma_{k,\pm}$ are related to the dispersion relation E_k in Eq. (3) of the main text by

$$\gamma_{k,\pm} \sim \frac{\kappa}{\delta}E_k. \tag{S6}$$

For example, for our $s = 0$ model, which has $\log_2(N/2)$ couplings of equal strength $J_\ell \equiv J$, the decay rates $\gamma_{k,\pm}$ are bounded above by

$$\gamma \lesssim \log_2(N/2)\frac{J\kappa}{\delta}. \tag{S7}$$

C. Interaction-to-Decay Ratio

We calculate an overall interaction-to-decay ratio at $s = 0$ by comparing the couplings J with the rates of collective decay γ via the cavity and spontaneous emission Γ_{sc}. We thus obtain a ratio

$$\rho \equiv \frac{J}{\gamma + B\Gamma_{\mathrm{sc},0}} \sim \frac{\beta}{\frac{M\beta\kappa}{\delta} + \frac{B\delta}{n\eta\kappa}}, \tag{S8}$$

where β is the modulation index for each sideband, $M \equiv \log_2(N/2)$ is the number of modulation frequencies, and $B = 1 + 2M\beta^2$. At an optimal detuning $\delta/\kappa \sim \sqrt{n\eta M\beta/B}$, we obtain

$$\rho = \frac{1}{2}\sqrt{\frac{n\eta\beta}{MB}} = \frac{1}{2}\sqrt{\frac{n\eta\beta/M}{1+2M\beta^2}}. \tag{S9}$$

Eq. (S9) is maximized by choosing the modulation index such that total power in the sidebands equals the power in the carrier, $2M\beta^2 = 1$, which is consistent with the weak-modulation requirement $\beta \ll 1$ provided that N is large. The interaction-to-decay ratio is then

$$\rho = \frac{\sqrt{n\eta}/2}{(2M)^{3/4}}. \tag{S10}$$

Reaching the scrambling time $Jt \sim 1$ requires an interaction-to-decay ratio $\rho \gtrsim 1$. By Eq. (S10), we thus require a large collective cooperativity of the subensemble at each site:

$$\frac{n\eta}{4} \gtrsim [2\log_2(N/2)]^{3/2}, \tag{S11}$$

where the weak scaling of the right-hand side with N is convenient for scaling to large system sizes. For example, Eq. (S10) can be satisfied for a system of $N = 2^{10}$ sites with $n = 300$ atoms per site and single-atom cooperativity $\eta \sim 1$ (Fig. S2). A higher but demonstrated single-atom cooperativity $\eta \sim 150$ [2] suffices to begin exploring fully quantum spin-1/2 models with a single atom per site.

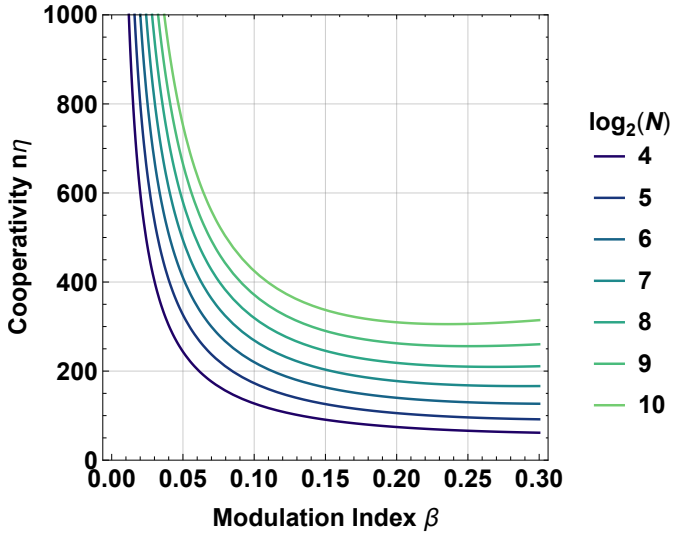

FIG. S2: **Cooperativity required to reach the scrambling time**, corresponding to an interaction-to-decay ratio $\rho = 1$. The required cooperativity $n\eta$ per subensemble is plotted as a function of modulation index β for system sizes ranging from $N = 2^4$ to $N = 2^{10}$ sites.

Even when these conditions on the cooperativity are satisfied, dissipation may modify shape of the light cone, as pointed out in Ref. [3]. This effect can be mitigated by measuring 'corrected' OTOCs [3, 4], which divide out the effects of dissipation and recover the shape of the true light cone.

D. Effects of Finite Modulation Depth

Our derivation of the couplings J_ℓ in Sec. I A assumes the conceptually simple limit of small modulation depth $\beta_\ell \ll 1$. In practice, for the system sizes most readily accessible in experiments, a finite modulation depth $\beta \sim 0.2$ is advantageous for maximizing the interaction-to-decay ratio (Fig. S2). Operating at finite modulation depth adds weak additional couplings (a factor β smaller than the intended couplings) at distances that are not powers of two. While these couplings are unlikely to appreciably alter the fast scrambling dynamics or the geometry of the coupling graph, it is worth noting that the modulation waveform can be designed to produce only the desired couplings even at finite modulation depth. In the most general case, for a control field $\Omega(t)$, the amplitude modulation waveform $|\Omega(t)|^2$ dictates the magnon dispersion relation $E(k) \propto |\Omega(k/\omega)|^2$. Thus, while the field $\Omega(t) \propto 1 + 2\sum_\ell \beta_\ell \cos(2^\ell \omega t)$ produces precisely the desired coupling pattern in the limit $\beta_\ell \ll 1$, a more general class of waveforms $\Omega(t) \propto \sqrt{E(\omega t) + \text{const.}}$ produce the same coupling pattern at finite modulation depth.

II. NUMERICAL AND ANALYTICAL TECHNIQUES

A. Magnon Occupation and Information Spreading

To characterize the spreading of local perturbations in the single-magnon sector, we introduce a single excitation at site i and evaluate the time t_ϵ at which the magnon occupation at another site j reaches a threshold value $\langle n_j \rangle = \epsilon = 1/N^2$. We note that the magnon occupation $\langle n_j(t) \rangle$, when the system is initialized with one excitation at site i, is equivalent to the OTOC

$$\langle n_j(t) \rangle = \langle 0 | c_i c_j^\dagger(t) c_j(t) c_i^\dagger | 0 \rangle = \langle 0 | [c_i, c_j^\dagger(t)][c_j(t), c_i^\dagger] | 0 \rangle \tag{S12}$$

since $c_j(t)|0\rangle = 0$. (Analogous relations hold for more general lowering operators A^-, B^-, so long as $B^-|0\rangle = 0$ and $|0\rangle$ is an eigenstate of H.) The occupation $\langle n_j(t) \rangle$ therefore encodes similar information about the spread of information in the system and is bounded by the Lieb-Robinson bound that controls the OTOC.

B. Characterizing Fastest- and Slowest-Growing Magnon Occupations

In Fig. S3, we plot the threshold time t_ϵ versus physical distance $d = |i - j|$ or Monna-mapped distance $d_{\mathcal{M}} = \mathcal{M}(d)$ from the original site for different values of s. While these plots show significant scatter, we observe that one can always bound the values t_ϵ from below by a polynomial light cone of the form

$$a \left[d_{(\mathcal{M})} \right]^b \leq t_\epsilon \tag{S13}$$

and from above by a function of the form

$$t_\epsilon \leq a' \left[d_{(\mathcal{M})} \right]^{b'} \left[\log d_{(\mathcal{M})} \right]^{c'} \tag{S14}$$

for some non-negative constants a, b, a', b', c'. To choose the lower-bound coefficients a, b optimally, we first fit Eq. (S13) to the fastest-growing occupations (black circles in Fig. S3), which always occur at distances $d_{(\mathcal{M})}$ that are powers of 2. The resulting lower bounds are shown in black in Fig. S3.

To find optimal upper-bound coefficients a', b', c', we first isolate the slowest-growing occupations by splitting the scatter plot into bins $d \in [2^n, 2^{n+1})$ for integers $0 \leq n \leq \log_2 N - 2$ and picking the largest value of t_ϵ within each bin (red diamonds in Fig. S3). We then use a constrained minimization search to find coefficients a', b', c' that minimize the sum of the squares of the differences between the slowest data points in each bin and the upper-bound function of Eq. (S14). In addition, to ensure that the resulting function bounds the slowest points from above, we place a constraint on the minimization search such that the optimal function must always lie *above* the slowest datapoints. Finally, to ensure that the upper and lower bounds Eqs. (S13) and (S14) hold simultaneously for large $d_{(\mathcal{M})}$, we demand that $a' \geq a$ and $b' \geq b$. The resulting optimal upper-bound curves are plotted in red in Fig. S3.

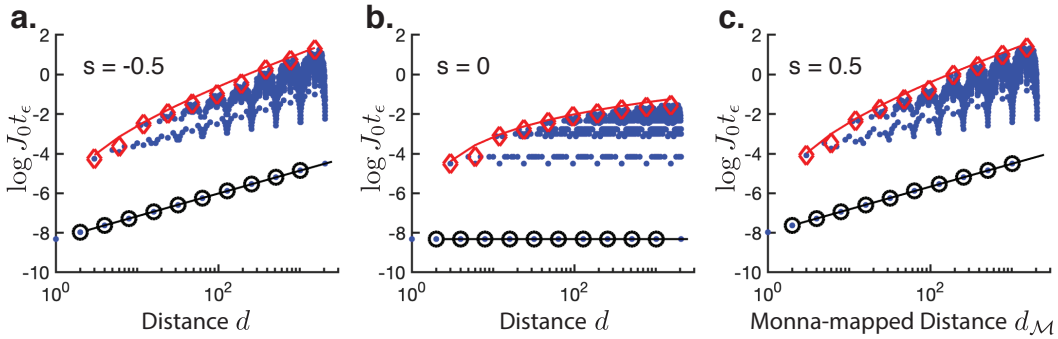

FIG. S3: **Upper and lower bounds on single-magnon occupation.** Time t_ϵ required for average magnon occupation $\langle n_{i+d}(t) \rangle$ to reach a fixed threshold ϵ vs physical distance d or Monna-mapped distance $d_{\mathcal{M}}$ for (a) $s = -0.5$, (b) $s = 0$, and (c) $s = 0.5$. Fastest-growing occupations (black circles) are bounded from below by a power-law in $d_{(\mathcal{M})}$ (black lines), while slowest-growing occupations (red diamonds) are bounded from above by the function (S14) (red lines).

C. Energy Level Statistics

To verify that the $s = 0$ model is chaotic in the interacting quantum regime, we calculate the energy level statistics for a system of $N = 16$ sites at half filling by exact diagonalization [5]. Figure S4 shows the distribution of spacings between neighboring energy levels, after unfolding the spectrum in each momentum sector according to the procedure in Ref. [6]. The distribution is consistent with the random-matrix statistics of the Gaussian Orthogonal Ensemble.

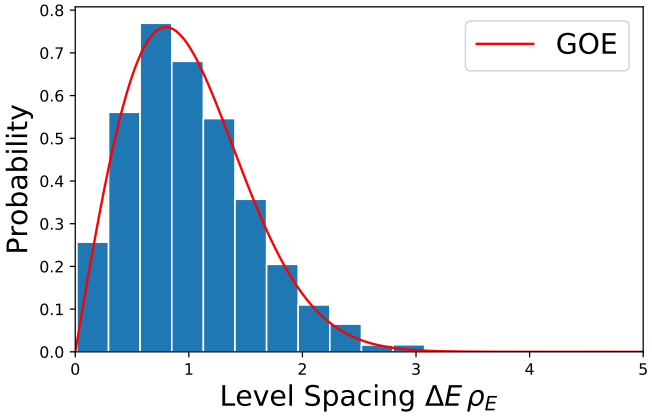

FIG. S4: **Chaotic level statistics.** Distribution of spacings between neighboring energy levels for the $s = 0$ model with $N = 16$ sites at half filling ($N/2$ magnons). The level spacings ΔE calculated for each momentum sector are normalized according to a Gaussian fit to the density of states ρ_E. Red curve shows the Wigner-Dyson distribution for the Gaussian Orthogonal Ensemble, indicating that the interacting system exhibits random-matrix statistics.

D. Short-Time Expansion of OTOCs

Here we show that OTOCs display power-law growth $C(t) \propto (Jt)^{2r_{ij}}$ at early times $Jt \ll 1$ [7], where J represents the typical energy scale of the Hamiltonian H. Consider the OTOC $C(i, j; t) = \langle [\mathcal{O}_i(t), \mathcal{O}_j(0)]^2 \rangle$, where $\mathcal{O}_i$ is an arbitrary operator at site i. At early times, the growth of OTOCs can be understood via a short-time expansion:

$$\mathcal{O}_i(t) = \mathcal{O}_i(0) - it[\mathcal{O}_i, H] - \frac{1}{2}t^2[[\mathcal{O}_i, H], H] + \cdots \tag{S15}$$

If there is a direct coupling between sites i and j, then at short times $t \ll J^{-1}$ the above expansion is simply dominated by the first two terms, leading to:

$$\langle [\mathcal{O}_i(t), \mathcal{O}_j(0)]^2 \rangle \approx t^2 \langle [[\mathcal{O}_i, H_{ij}], \mathcal{O}_j]^2 \rangle \tag{S16}$$

where H_{ij} is the term in the Hamiltonian coupling sites $i \neq j$. If there is no direct coupling between i, j, then this lowest-order quadratic term vanishes and we must consider higher-order terms in the expansion. More generally, if r_{ij} is the minimum number of couplings H_{nm} required to hop from site i to site j, then all lowest-order terms $\sim t^{2n}$ for $n < r_{ij}$ vanish, and the early-time growth is dominated by

$$C(i, j; t) \propto (Jt)^{2r_{ij}} \tag{S17}$$

where the constant of proportionality includes contributions from nested commutators $\langle [[[[\mathcal{O}_i, H], H], \ldots, H], \mathcal{O}_j]^2 \rangle$. For example, for the interaction graph at $s = 0$, we find that $C(0, 1; t)$ and $C(0, 2; t)$ grow like $(J_0 t)^2$ at early times since there is a direct coupling between sites $0, 1$ and sites $0, 2$. Similarly, $C(0, 3; t)$ grows like $(J_0 t)^4$ because it requires two couplings to hop between sites 0 and 3, and $C(0, 11; t)$ grows like $(J_0 t)^6$ because it requires three couplings to hop between sites 0 and 11.

E. Semiclassical Numerics

While exact diagonalization and Matrix Product State techniques can give us access to the full quantum dynamics of the Hamiltonian (1), these techniques limit us to relatively small system sizes. To examine information spreading in

larger system sizes while retaining access to strong interactions and chaos, we must resort to a semiclassical treatment by considering the limit where the spin lengths $S \to \infty$ [8]. In this limit, each spin operator $\mathbf{S}_i$ can be understood as a classical angular momentum vector obeying the Poisson bracket algebra:

$$\left\{S_i^\alpha, S_j^\beta\right\} = \sum_\gamma S_i^\gamma \epsilon^{\alpha\beta\gamma}\delta_{ij} \tag{S18}$$

and whose equations of motion are given by

$$\dot{S}_i^\alpha = \{S_i^\alpha, H\} \ . \tag{S19}$$

Defining unit-length spin vectors $\mathbf{x}_i = \mathbf{S}_i/S$ and taking the limit $S \to \infty$, we obtain classical equations of motion of the form:

$$\dot{\mathbf{x}}_i = f(\mathbf{x}_i) \tag{S20}$$

where f is a quadratic function of the spin vectors $\mathbf{x}_i$ that depends on the coupling graph $J(i-j)$ but is independent of S.

To mimic an infinite-temperature quantum state consisting of exactly $N/2$ magnons, we prepare the spins along random directions in the $x-y$ plane. (Preparing spins with additional out-of-plane fluctuations in the z-direction, or with uniformly random directions, has no significant effect on the dynamics.) We then estimate the classical sensitivity $C_{\rm cl}(t)$ by perturbing a single spin at site i by a small rotation ϕ_i about the z axis, and measure the resulting change $\Delta\mathbf{x}_j(t)$ in spin j at a later time t.

F. Simulating OTOCs with Matrix Product Operators

Here we describe how OTOCs are calculated using tensor network methods. We perform simulations with Matrix Product States and Operators (MPS/MPO) [9], which a regularly used to successfully simulate quantum many-body dynamics in one dimensional systems [10, 11]. Although here we have only made use of MPS and MPO techniques, in future work it might be beneficial to try other generalized forms of tensor networks for treating these sparse models, such as the Tree Tensor Network [12] or the Multi-scale Entanglement Renormalization Ansatz [13]. These may account more naturally for the geometry of long-range sparse interactions between spins.

In our calculations, we consider the symmetry sector of the Hilbert space of N spins with a fixed number of magnons, n. The initial state of the system ρ_0 is the infinite-temperature state within this symmetry sector, and may be written as $\rho_0 = P_n/\mathcal{Z}$, where the P_n is the projector on states with n magnons and $\mathcal{Z}$ is the partition function, which in the case of infinite temperature is equal to the number of permutations of n magnons on N sites.

We construct the projector P_n as an MPO by writing it as a product of $n \times n$ matrices,

$$P_n = \mathcal{B}_n^{[1]}\mathcal{B}_n^{[2]}...\mathcal{B}_n^{[N]}, \tag{S21}$$

where

$$\begin{aligned}
\mathcal{B}_n^{[1]} &= \begin{pmatrix} p_\downarrow & p_\uparrow & 0 & 0 & \dots \end{pmatrix}, \\
\mathcal{B}_n^{[1<i<N]} &= \begin{pmatrix} p_\downarrow & p_\uparrow & 0 & 0 & \dots \\ 0 & p_\downarrow & p_\uparrow & 0 & \\ 0 & 0 & p_\downarrow & p_\uparrow & \\ 0 & 0 & 0 & p_\downarrow & \\ \vdots & & & & \ddots \end{pmatrix}, \\
\mathcal{B}_n^{[N]} &= \begin{pmatrix} \vdots \\ 0 \\ 0 \\ p_\uparrow \\ p_\downarrow \end{pmatrix},
\end{aligned} \tag{S22}$$

are constructed out of operators $p_\downarrow = |\downarrow\rangle\langle\downarrow|$ and $p_\uparrow = |\uparrow\rangle\langle\uparrow|$ acting on local spins.

Having constructed this infinite temperature state, the next step is to time evolve the operator $S_j^z(t)$ from Eq. (5) in the Heisenberg picture. In order to do this, we combine the local indices of the operator, thus vectorizing it so that it can be propagated in time using the same techniques we apply for MPS. We find that using a TDVP [14–17] provides

a good balance between speed and accuracy in this calculation (although for some purposes, using the Runge-Kutta method [10] could yield higher accuracy). After the time evolution, we separate out the local indices of $S^z_j(t)$ and contract it with $S^z_i(0)$ and ρ_0 to obtain $C(i,j;t)$ in Eq. (5).

[1] E. J. Davis, G. Bentsen, L. Homeier, T. Li, and M. H. Schleier-Smith, Phys. Rev. Lett. **122**, 010405 (2019).
[2] Y. Colombe, T. Steinmetz, G. Dubois, F. Linke, D. Hunger, and J. Reichel, Nature **450**, 272 (2007).
[3] Y.-L. Zhang, Y. Huang, and X. Chen, Phys. Rev. B **99**, 014303 (2019).
[4] B. Swingle and N. Yunger Halpern, Phys. Rev. A **97**, 062113 (2018).
[5] P. Weinberg and M. Bukov, SciPost Phys. **2**, 003 (2017).
[6] S. Wimberger, Nonlinear Dynamics and Quantum Chaos (Springer International Publishing, 2014).
[7] J. Marino and A. Rey, Physical Review A **99**, 051803(R) (2019).
[8] A. Polkovnikov, Ann. Phys. (N. Y.) **325**, 1790 (2010).
[9] U. Schollwoeck, Ann. Phys. (N. Y.) **326**, 96 (2011).
[10] J. J. García-Ripoll, New J. Phys. **8**, 305 (2006).
[11] S. Paeckel, T. Köhler, A. Swoboda, S. R. Manmana, U. Schollwöck, and C. Hubig, (2019), arXiv:1901.05824 .
[12] Y.-Y. Shi, L.-M. Duan, and G. Vidal, Phys. Rev. A **74**, 022320 (2006).
[13] G. Vidal, Phys. Rev. Lett. **101**, 110501 (2008).
[14] J. Haegeman, J. I. Cirac, T. J. Osborne, I. Pižorn, H. Verschelde, and F. Verstraete, Phys. Rev. Lett. **107**, 070601 (2011).
[15] T. Koffel, M. Lewenstein, and L. Tagliacozzo, Phys. Rev. Lett. **109**, 267203 (2012).
[16] J. Haegeman, T. J. Osborne, and F. Verstraete, Phys. Rev. B **88**, 075133 (2013).
[17] J. Haegeman, C. Lubich, I. Oseledets, B. Vandereycken, and F. Verstraete, Phys. Rev. B **94**, 165116 (2016).